The Astrophysical Journal Supplement Series, 257:31 (11pp), 2021 December https://doi.org/10.3847/1538-4365/ac1d43

The mini-JPAS: A Study of the Wavelength Dependence of the Photon Response Nonuniformity of the JPAS-Pathfinder Camera

Kai Xiao[1], Haibo Yuan[1], J. Varela[2], Hu Zhan[3,4], Jifeng Liu[5], R. Abramo[6], J. Alcaniz[7], N. Benitez[8], S. Bonoli[9,10], S. Carneiro[11], J. Cenarro[2], D. Cristóbal-Hornillos[9], C. M. de Oliveira[12], R. Dupke[7], A. Ederoclite[12], C. López-Sanjuan[2], A. Marín-Franch[2], M. Moles[2], A. Moreno[2], D. Muniesa[2], L. Sodré, Jr.[12], K. Taylor[13], and H. Vázquez-Ramió[2]
[1] Department of Astronomy, Beijing Normal University, Beijing, 100875, People's Republic of China; yuanhb@bnu.edu.cn
[2] Centro de Estudios de Física del Cosmos de Aragón (CEFCA), Unidad Asociada al CSIC, Plaza San Juan 1, 44001, Teruel, Spain
[3] Key Laboratory of Space Astronomy and Technology, National Astronomical Observatories, Chinese Academy of Sciences, Beijing 100101, People's Republic of China
[4] Kavli Institute for Astronomy and Astrophysics, Peking University, Beijing 100871, People's Republic of China
[5] National Astronomical Observatories, Chinese Academy of Sciences, 20A Datun Road, Chaoyang District, Beijing, People's Republic of China
[6] Instituto de Física, Universidade de São Paulo, 05508-090, São Paulo, SP, Brazil
[7] Observatório Nacional, Ministério da Ciencia, Tecnologia, Inovação e Comunicações, 20921-400, Rio de Janeiro, RJ, Brazil
[8] Instituto de Astrofísica de Andalucá—CSIC, Apdo 3004, E-18080, Granada, Spain
[9] Centro de Estudios de Física del Cosmos de Aragón (CEFCA), Plaza San Juan 1, 44001 Teruel, Spain
[10] Donostia International Physics Center (DIPC), Manuel Lardizabal Ibilbidea, E-4, San Sebastián, Spain
[11] Instituto de Física, Universidade Federal da Bahia, 40210-340, Salvador, BA, Brazil
[12] Departamento de Astronomia, Instituto de Astronomia, Geofísica e Ciências Atmosféricas, Universidade de São Paulo, 05508-090, São Paulo, SP, Brazil
[13] Instruments4, 4121 Pembury Place, La Cañada Flintridge, CA 91011, USA
Received 2021 June 10; revised 2021 August 3; accepted 2021 August 11; published 2021 November 12

Abstract

Understanding the origins of small-scale flats of CCDs and their wavelength-dependent variations plays an important role in high-precision photometric, astrometric, and shape measurements of astronomical objects. Based on the unique flat data of 47 narrowband filters provided by JPAS-Pathfinder, we analyze the variations of small-scale flats as a function of wavelength. We find moderate variations (from about 1.0% at 390 nm to 0.3% at 890 nm) of small-scale flats among different filters, increasing toward shorter wavelengths. Small-scale flats of two filters close in central wavelengths are strongly correlated. We then use a simple physical model to reproduce the observed variations to a precision of about ±0.14% by considering the variations of charge collection efficiencies, effective areas, and thicknesses between CCD pixels. We find that the wavelength-dependent variations of the small-scale flats of the JPAS-Pathfinder camera originate from inhomogeneities of the quantum efficiency (particularly charge collection efficiency), as well as the effective area and thickness of CCD pixels. The former dominates the variations in short wavelengths, while the latter two dominate at longer wavelengths. The effects on proper flat-fielding, as well as on photometric/flux calibrations for photometric/slitless spectroscopic surveys, are discussed, particularly in blue filters/wavelengths. We also find that different model parameters are sensitive to flats of different wavelengths, depending on the relations between the electron absorption depth, photon absorption length, and CCD thickness. In order to model the wavelength-dependent variations of small-scale flats, a small number (around 10) of small-scale flats with well-selected wavelengths are sufficient to reconstruct small-scale flats in other wavelengths.

Unified Astronomy Thesaurus concepts: CCD observation (207); CCD photometry (208); Flux calibration (544); Astronomy data reduction (1861)

1. Introduction

Charge-coupled devices (CCDs) are widely used in astronomical surveys, such as the Sloan Digital Sky Survey (York et al. 2000), the ongoing Dark Energy Survey (Wester & Dark Energy Survey Collaboration 2005; DESI Collaboration et al. 2016), the upcoming Javalambre Physics of the Accelerating Universe Astrophysical Survey (JPAS; Benitez et al. 2014), the Multi-channel Photometric Survey Telescope (X. Er et al., in preparation), the Vera Rubin Observatory (LSST Science Collaboration et al. 2009), the China Space Station Telescope (Zhan 2011, 2021), the Nancy Grace Roman Space Telescope (McEnery 2021), and the ESA Euclid telescope (Racca et al. 2016). To achieve the various demanding goals of the above projects, precise measurements of the brightness, position, and shape of astronomical objects are needed, requiring proper treatment of instrumental systematics affecting photometry, astrometry, and object shape measurements.

Flat-fielding is one of the most challenging steps in image processing of wide-field surveys. It plays a key role in correcting for instrumental systematics and limiting the precision of the photometric calibration (e.g., Stubbs & Tonry 2006). The contributions of flat-fielding can be decomposed into two parts: the large-scale flat and the small-scale flat. The former, sometimes known as illumination correction, is mainly caused by the optical system of telescopes (such as the vignetting effect and field distortion) and the nonuniform coating of CCD detectors, while the latter, named pixel-response nonuniformity (PRNU), is generally related to the inhomogeneities of the quantum efficiency between adjacent CCD pixels, assuming that all CCD pixels have the same size and are uniformly distributed. However, recent studies have shown that the variations of the effective area of the pixel (pixel-to-pixel size variations) play an important role in determining the PRNU of some CCD detectors (Baumer et al. 2017 and references therein). In this case, dividing a raw

image by a flat-field image is no longer valid for flat-fielding correction. To better understand the nature of the PRNU of CCD detectors, the dependences of PRNU on wavelength are very essential.

The JPAS aims to image thousands of square degrees of the northern sky with a unique set of 54 narrowband filters, covering 3785–9100 Å, using a dedicated 2.55 m telescope, JST/T250, at the Javalambre Astrophysical Observatory (Bonoli et al. 2021).[14] In its commissioning phase, a pathfinder camera was first installed to test the telescope performance and execute the first scientific operations.

A large number of sky-flat images in each filter have been obtained, providing a unique data set to investigate the wavelength-dependent PRNU of the JPAS-Pathfinder camera.

In this work, small-scale flat-field images for each narrowband filter are computed from coadded flat-field images and then used to study the wavelength-dependent PRNU of the JPAS-Pathfinder camera. A simple physical model is constructed to parameterize/reproduce the variations of small-scale flats as a function of wavelength, taking into account the variations of quantum efficiencies (caused by charge collection efficiencies), pixel sizes, and depths.

The paper is organized as follows. In Sections 2 and 3, we introduce the data and model used in this work. The results are presented in Section 4 and discussed in Section 5. A summary is given in Section 6.

2. Data

The JPAS-Pathfinder camera, located at the center of the JST/T250 field of view, is equipped with a single large, 9216×9232 CCD290-99 detector from Teledyne e2V. The detector has 16 outputs for fast readout. It has an imaging area of 92.16 mm × 92.32 mm, corresponding to a 0.27 $\deg^2$ field of view. The pixel size is 10 μm, and the depth is 40 μm. A broadband antireflective coating is adopted to optimize performance from 380 to 850 nm. Other technical parameters of the detector can be found in Table 2 of Bonoli et al. (2021).

The novel and unique aspect of JPAS lies in its filter system: 54 narrowband filters ranging from 3780 to 9100 Å, complemented with two broader filters in the blue and red wavelength regions. The narrowband filters have an FWHM of 145 Å and are spaced by about 100 Å (except for the filter J0378), thus covering the entire optical range. The blocking of the filters is better than OD5 (transmission $<10^{-5}$) in the range 250–1050 nm (Brauneck et al. 2018); therefore, the photometric leakage in the filter bandpasses is not important. The JPAS filters have also been designed to minimize internal reflections. The intensity of the parasitic scattering light shall be at least 6 orders of magnitude smaller than the incident light. These low internal reflections are not measurable in real images (Brauneck et al. 2018).

Due to the low sky background of the narrowband filters, the CCD scientific images are read out in a 2×2 binning mode to reduce the readout noise, as were the flat images. Therefore, each pixel in the flat images corresponds to four physical pixels.

Twilight flats are used for the flat-fielding of mini-JPAS observations. Several to tens of sky flats are usually obtained for each filter and then coadded to obtain the master flat after bias subtraction.

The typical signal-to-noise ratios (S/Ns) are about 1000 pixel^{-1}. For each master flat, the large-scale flat is estimated by a running mean filter smoothing with a window size of 50×50 pixels. The small-scale flat is obtained by dividing the original flats by the large-scale one.

The numbers of exposures for different filters are listed in Table 1. The flats for three filters (J0800, J0810, and J0820) are excluded in the current work due to low S/Ns. The flats of another three filters (J0900, J0910, and J1007) are also excluded due to strong fringing patterns in the flat images. The J0360 flat is excluded due to its wider wavelength

[14] https://j-pas.org

Table 1
Number of Exposures for Different Filters

Filter	Number	Filter	Number	Filter	Number
J0390	17	J0590	36	J0800[a]	5
J0400	52	J0600	17	J0810[a]	7
J0410	36	J0610	34	J0820[a]	10
J0420	30	J0620	36	J0830	17
J0430	29	J0630	37	J0840	17
J0440	65	J0640	29	J0850	17
J0450	50	J0650	83	J0860	42
J0460	17	J0660	32	J0870	55
J0470	46	J0670	17	J0880	55
J0480	35	J0680	35	J0890	55
J0490	32	J0700	60	J0900[b]	57
J0500	25	J0710	29	J0910[b]	56
J0510	62	J0720	74	J1007[b]	54
J0520	51	J0730	37		
J0530	17	J0740	17		
J0540	46	J0750	54		
J0550	36	J0760	36		
J0560	31	J0770	60		
J0570	34	J0780	29		
J0580	79	J0790	71		

Notes.
[a] Not used due to a small number of exposure times.
[b] Not used due to fringing patterns.

Table 2
Photon Absorption Length at Different Wavelengths of Si at −100°C (Rajkanan et al. 1979; Green & Keevers 1995)

λ (nm)	L (μm)	λ (nm)	L (μm)	λ (nm)	L (μm)
250	0.006409	460	0.8082	670	6.916
260	0.005938	470	0.9823	680	7.479
270	0.005326	480	1.125	700	8.776
280	0.004886	490	1.277	710	9.466
290	0.005116	500	1.424	720	10.14
300	0.006589	510	1.621	730	10.99
310	0.007883	520	1.790	740	11.99
320	0.008840	530	2.011	750	13.17
330	0.009656	540	2.245	760	14.48
340	0.01037	550	2.482	770	15.77
350	0.01091	560	2.751	780	17.30
360	0.01124	570	2.996	790	18.97
370	0.01685	580	3.27	830	28.23
380	0.04285	590	3.569	840	31.24
390	0.09592	600	3.882	850	34.93
400	0.1713	610	4.231	860	39.43
410	0.2438	620	4.594	870	44.44
420	0.3314	630	4.961	880	50.90
430	0.4263	640	5.355	890	57.82
440	0.5414	650	5.814		
450	0.6642	660	6.356		

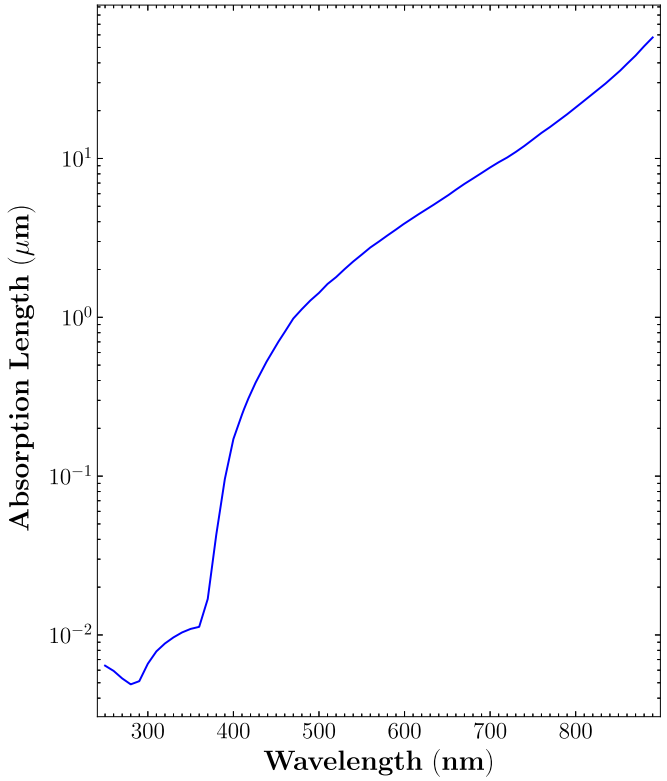

Figure 1. Dependence on the wavelength of the absorption length in Si at −100°C (Rajkanan et al. 1979; Green & Keevers 1995).

coverage. Above, in total, the flats of 47 narrowband filters are used for the calculation of small-scale variation.

3. Model

The PRNU of the CCDs can be analyzed from the perspective of the photovoltaic conversion process. Ignoring the charge loss during the charge transfer process, the electrical signal generated on a CCD pixel by monochromatic light can be expressed as

$$I_{\rm i} = \frac{1}{\rm gain}\frac{\eta_{\rm i} A_{\rm i}}{h\nu}\int_t E dt, \tag{1}$$

where $\eta_{\rm i}$ and $A_{\rm i}$ are the quantum efficiency and effective area of the ith pixel, respectively, and h, ν, E, and t are the Planck constant, frequency of radiated photons, irradiance of the CCD surface, and exposure time, respectively. The gain of a CCD is set by the output electronics and determines how the number of charges collected in each pixel will be assigned to a digital number in the output image (e.g., Howell 2006).

The quantum efficiency of a CCD pixel can be expressed as

$$\eta_{\rm i} = \alpha {\rm CCE_i}(1-R)(1-e^{-H_{\rm i}/L}), \tag{2}$$

where α is the quantum yield, which is related to photon energy; $\rm CCE_i$ is the charge collection efficiency; R is the reflectivity of the CCD; $H_{\rm i}$ is the thickness of the silicon photosensitive layer; and L is the photon absorption length (Janesick et al. 1985; Janesick 2007).

Verhoeve et al. (2014) found that small-scale flats show much larger variations in shorter wavelengths for a backside-illuminated CCD. Its PRNU is dominated by the residual step pattern of imperfect ion implantation and laser annealing. The pattern is strongest at the shortest wavelengths, for which the photon absorption depth is shallowest. Therefore, it is likely that the PRNU in the near-ultraviolet and blue is dominated by nonuniform trapping or recombination of photon-generated electrons in the very top layer of the CCD back surface (i.e., those "partial events" defined in Janesick et al. 1985), which may be thought of as an effective absorption. Based on this assumption, B. Chen & H. Zhan (2021, private communication) and W. Du et al. (2021, in preparation) proposed four models of $\rm CCE_i$ to describe the probability of the electrons being "absorbed" as a function of depth in the thin layer. The models were tested using flat fields in the lab in wavelengths from 360 to 625 nm. It was found that the model assuming the probability of an electron to be absorbed following an exponential decay matches the data best. Therefore, we adopt the same model in this work. According to the exponential decay model, the charge collection efficiency of the ith pixel can be written as

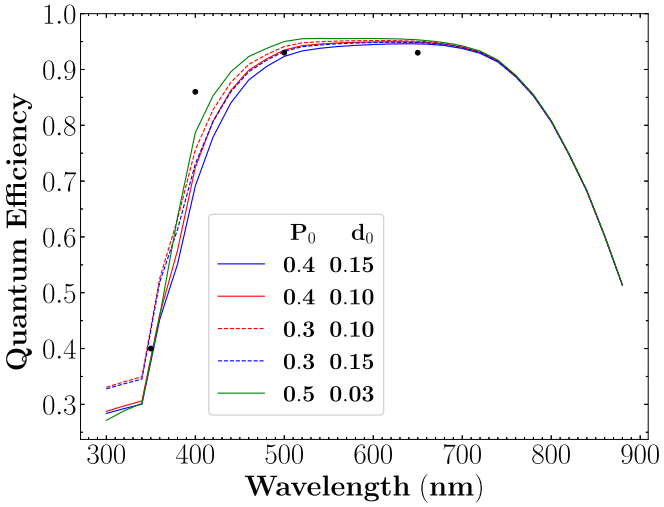

Figure 2. Quantum efficiency as a function of wavelength for different [P, d] combinations, assuming typical antireflectivity coating efficiency factors. The black dots are the quantum efficiencies of the mini-JPAS camera (Table 2 in Bonoli et al. 2021).

$$\rm CCE_i = 1 - \frac{P_i d_i}{L + d_i}\frac{1 - e^{-(L+d_i)H_i/Ld_i}}{1 - e^{-H_i/L}}, \tag{3}$$

where d is the decay scale length and P is the probability of being absorbed per unit depth at the CCD surface.

Equations (1)–(3) are in dimensional form. If we neglect the CCD reflectivity nonuniformity, which is probably not important on the 50×50 pixel scales, and we adopt the mean electrical signal of each pixel, $\bar{I} = \frac{1}{N}\sum_{\rm i=0}^{N-1} I_{\rm i}$, as a normalizing constant, we can obtain the dimensionless equation from Equations (1)–(3) as

$$\frac{I_{\rm i}}{\bar{I}} = \frac{A_{\rm i}{\rm CCE_i}(1-e^{-H_{\rm i}/L})}{\frac{1}{N}\sum_{\rm i=0}^{N-1} A_{\rm i}{\rm CCE_i}(1-e^{-H_{\rm i}/L})}. \tag{4}$$

For a given wavelength, the photon absorption length in Si depends only on temperature. A theoretical calculation of temperature-dependent photon absorption lengths was given in Rajkanan et al. (1979). The actual measured values of the photon absorption lengths in Si at 300K can be found in Green & Keevers (1995). However, at most wavelengths for this work, the discrepancies between the calculated and measured photon absorption lengths at 300K are larger (by about 30%).

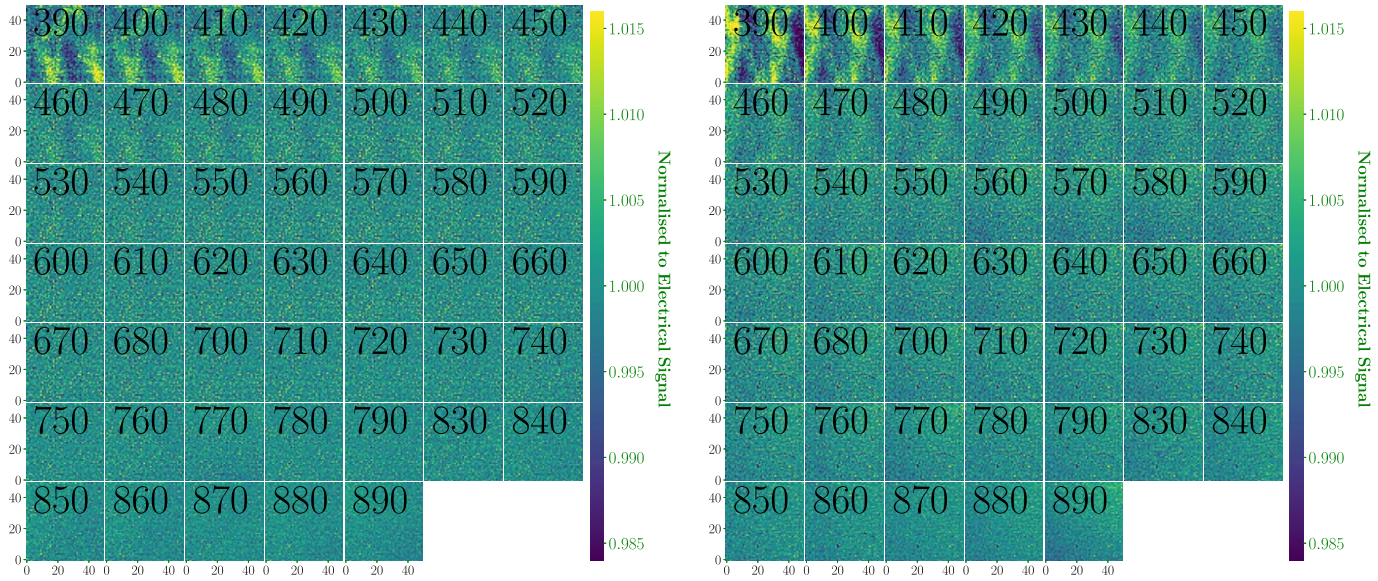

Figure 3. Small-scale flats at 47 wavelengths for selected areas are composed of 50 × 50 pixels. The left panel is for the center region (*X* from 1786 to 1836 pixels and *Y* from 2132 to 2182 pixels), and the right panel is for the lower left corner (*X* from 245 to 295 pixels and *Y* from 245 to 295 pixels).

Therefore, assuming that the differences do not depend on temperature, the photon absorption lengths used in this work are obtained as follows. We first calculate the theoretical ratios between the photon absorption lengths at 173 K (the working temperature of the mini-JPAS camera) and 300 K, then multiply by the measured photon absorption lengths at 300 K. The adopted photon absorption lengths of Si at 173 K as a function of wavelength are given in Table 2 and plotted in Figure 1. It can be seen that the absorption length does not vary substantially for wavelengths between 250 and 370 nm but increases rapidly to 420 nm and then more slowly to 890 nm.

For a given wavelength, there are only four free parameters (P_i, d_i, H_i, and A_i) for a given pixel in Equation (4). Therefore, the values of these parameters are possibly well constrained by a small number ($\geqslant$4) of small-scale flats. This provides the possibility that a small number ($\geqslant$4) of small-scale flats with well-selected wavelengths are sufficient to reconstruct small-scale flats in other wavelengths. Note that A_i is the effective area and is used to account for wavelength-independent variations of small-scale flats. The variations of A_i do not necessarily mean the variations in physical size.

In order to determine the underlying parameters based on observational data, an initial set of parameter values (*P*, *d*, *H*, and *A*) are needed as reference, particularly *P* and *d*. The *H* and *A* reference values are set to be 40 μm and 20 μm × 20 μm, respectively. For *P* and *d*, their reference values are constrained by the quantum efficiency curve of the CCD used. This is because the quantum efficiency curve in blue wavelengths for a given CCD depends on not only its reflectivity curve after coating but also its typical *P* and *d* values. Figure 2 plots the quantum efficiencies at four wavelengths of the mini-JPAS CCD. The predicted quantum efficiency curves of different [*P*, *d*] combinations are overplotted, assuming typical wavelength-dependent antireflectivity coating efficiency factors from Table 2.1 from Janesick (2007).[15] Finally, we choose the reference values of *P* and *d* to be 0.40 and 0.10 μm, respectively. Due to the lack of measured quantum efficiencies and reflectivity curves, the *P* and *d* reference values are not well constrained. We will discuss the effect of different *P* and *d* reference values in Section 5.

[15] The true reflectivity curve is unknown.

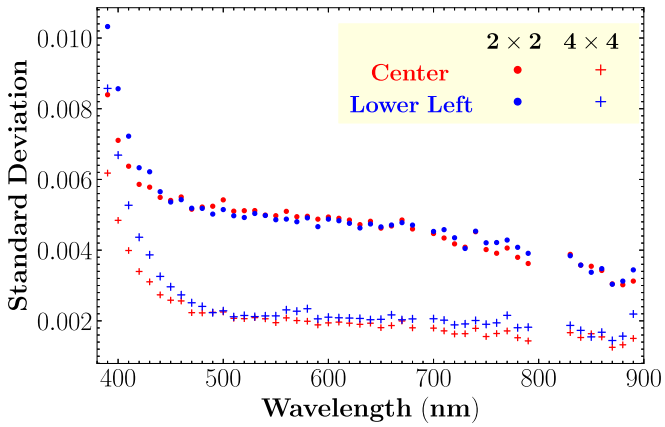

Figure 4. Standard deviations of small-scale flats as a function of wavelength. The red and blue symbols are for the center and lower left corner regions, respectively. The dots denote results after a 2 × 2 binning during the readout process. The plus signs denote results in an additional 2 × 2 binning after readout, i.e., 4 × 4 binning in physical pixels.

Given the reference values of the CCD, the *P*, *d*, *H*, and *A* values for each pixel are estimated by minimizing the differences between the observed and modeled small-scale flats. A Python package for sequential least-squares programming (Kraft 1998) is used in the optimization process.

4. Results

Figure 3 shows the small-scale flats we obtained at 47 wavelengths. Two small regions of 50 × 50 pixels are selected, including one in the center and one in the lower left corner of the CCD. For both regions, the bluer the filter, the larger the scatter. The trend is more clearly displayed in Figure 4. The

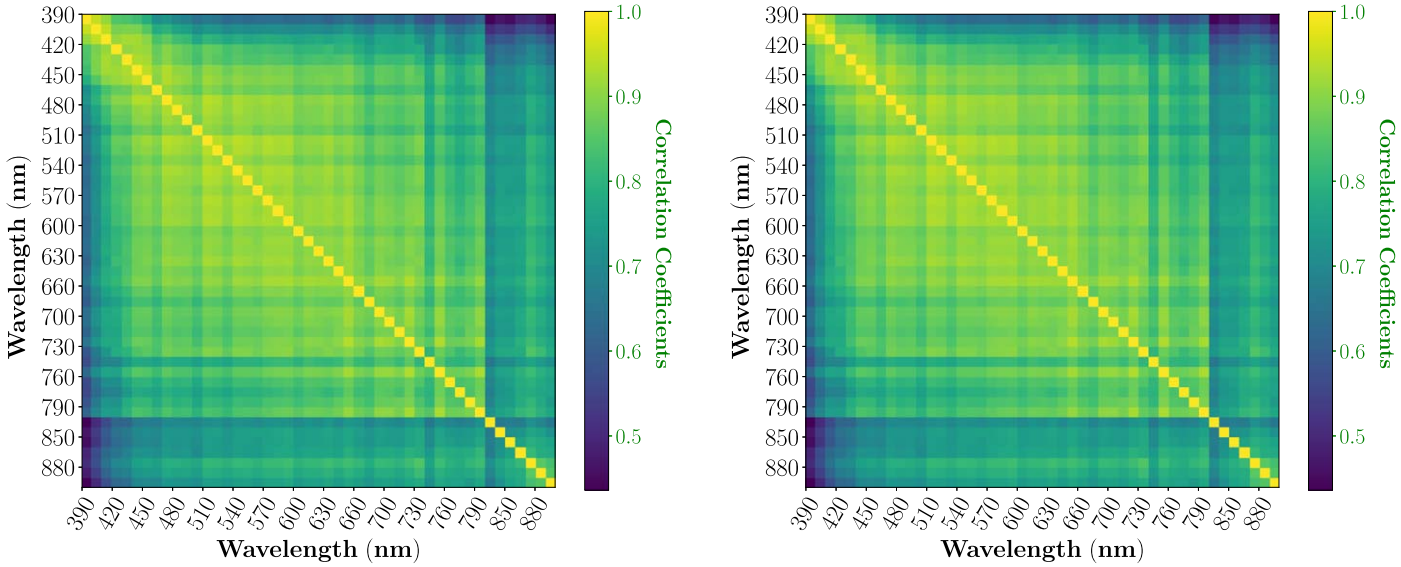

Figure 5. Correlation coefficients between the small-scale flats of two filters. The left and right panels are for the center and lower left corner regions, respectively.

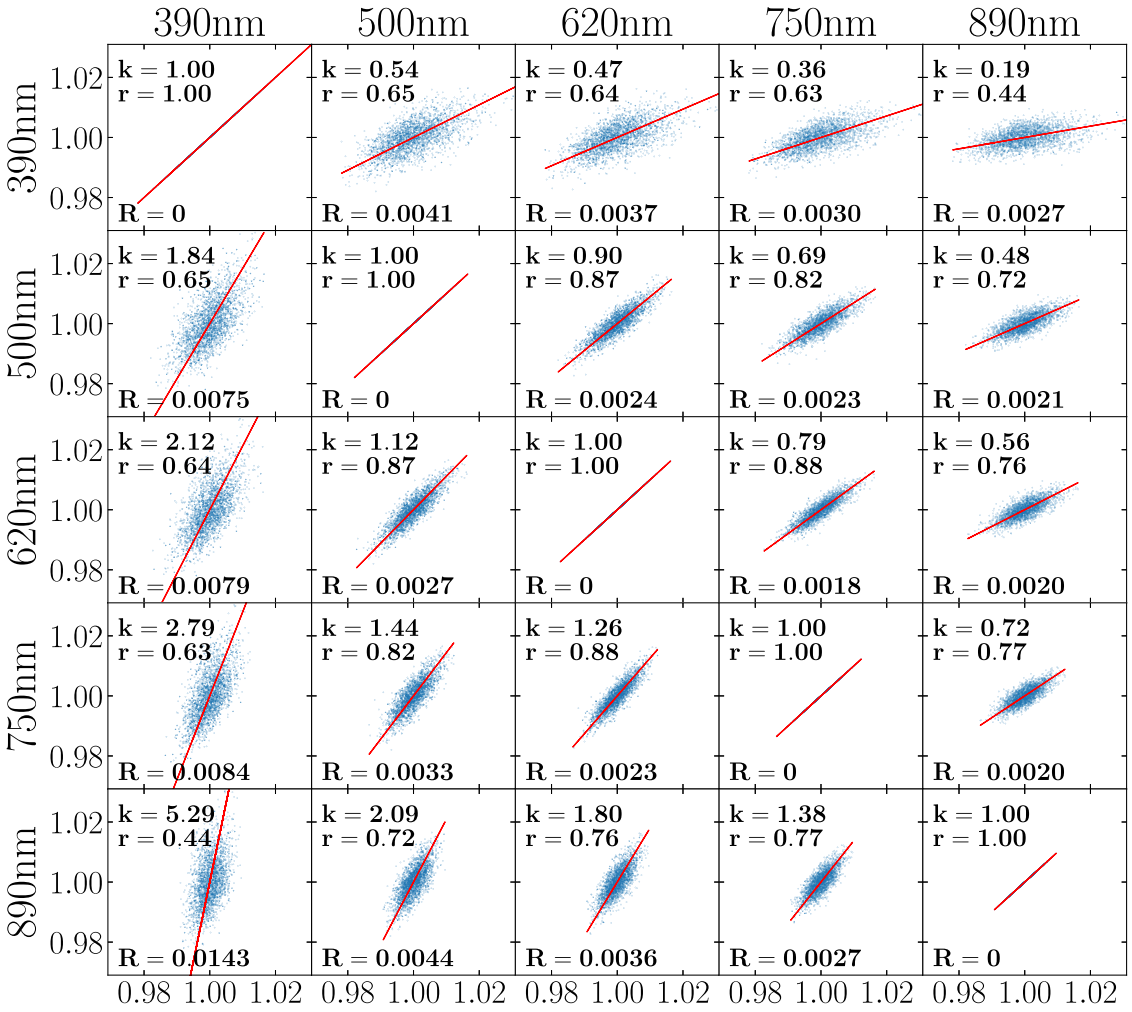

Figure 6. Examples of correlation plots between the small-scale flats of two filters in the center region. The filter central wavelengths are labeled. For each panel, the red line denotes the linear fitting result. The slope (k), correlation coefficient (r), and fitting residual (R) are marked.

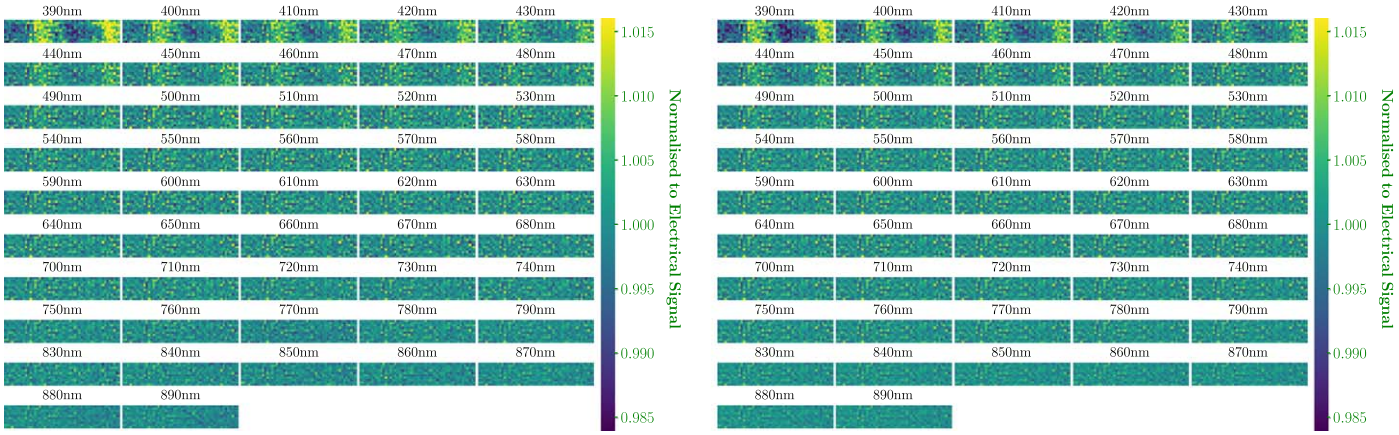

Figure 7. Observed (left panel) and modeled (right panel) small-scale flats of the center region.

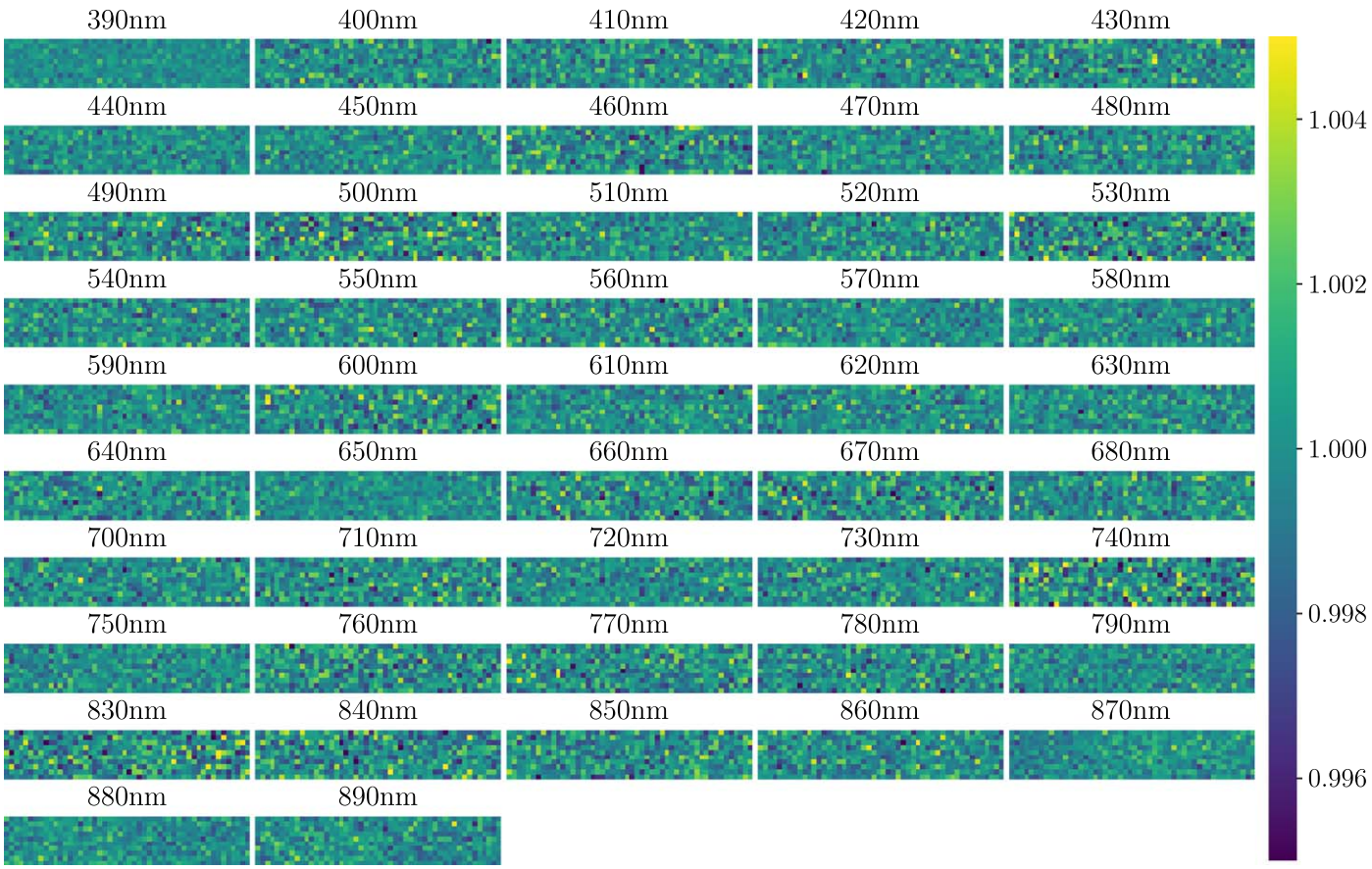

Figure 8. Ratios of the observed to modeled small-scale flats of the center region.

standard deviation values decrease rapidly from about 1.0% at 390 nm to 0.55% at 440 nm, then slowly to 0.3% at 890 nm. To investigate the effect of binning, the standard deviation values after another 2×2 binning are overplotted. The values decrease significantly for wavelengths longer than around 450 nm but slightly for shorter wavelengths. This implies that if no binning was performed during the readout process, the standard deviation values would increase to some extent for wavelengths longer than around 450 nm but slightly for shorter wavelengths. Note that the standard deviations for the lower left corner are always slightly higher in the 4×4 binning. We have checked the standard deviations for the other three corners; it is not always the case that the values are higher in the corner regions.

Further, we perform a linear fitting for the normalized electrical signal sets at 2500 pixels between the small-scale flats from any two filters and estimate their correlation coefficients. The correlation coefficients are displayed in Figure 5. When the two filters are closer in wavelength, the correlations are usually stronger, and the slopes are closer to 1. Note that the grid

pattern in Figure 5 is not real. It is mainly due to the relatively lower S/Ns (numbers of exposure times) of the flats of several filters (e.g., at 460, 530, 600, 670, 740, 830, 840, and 850 nm). Examples of the correlations are shown in Figure 6. The result suggests that the small-scale flats are more similar when the center wavelengths are closer.

We now apply our model to fit the observed small-scale flats. In order to reduce the number of free parameters and computing time, we further select a smaller region of 10×50 pixels from the left panel of Figure 3, as shown in the left panel of Figure 7.[16] The selected data are used to constrain our model, which has a total of $10 \times 50 \times 4$ free parameters. The right panel of Figure 7 shows the model results, which agree well with the observations. Detailed comparisons between the observed and modeled flats are displayed in Figure 8. The standard deviations of their ratios are plotted in Figure 9. It can be seen that our model reproduces the observed small-scale flats well in all wavelengths. The median standard deviation is only 0.14%. Note that the standard deviations show a moderate anticorrelation with the number of exposure times, suggesting that a large fraction of the scatters are contributed by random errors in the flats.

The model parameters are normalized by their corresponding reference values. Figure 10 shows the histogram distributions of the four normalized parameters (P', d', A', and H'). The normalized parameters roughly follow Gaussian distributions, with sigma values of 3.8%, 6.0%, 0.44%, and 0.39% for P', d', A', and H', respectively. The distributions of $P' \cdot d'$ and $A' \cdot H'$ are also plotted in Figure 10, with sigma values of 4.9% and 0.22%, respectively.

To investigate the sensitivities of different model parameters on flats in different wavelengths, the correlation coefficients between model parameters (P, d, A, H, $P \cdot d$, and $A \cdot H$) and observed small-scale flats are plotted against wavelength in Figure 11. The correlation coefficient for the $A \cdot H$ parameter increases with wavelength, reaching a peak value of about 0.75 at 880 nm. The correlation coefficient for the area parameter A peaks at a medium wavelength around 650 nm. The correlation coefficients for both P and d parameters are small for all of the available wavelengths, while the $P \cdot d$ parameter has a strong negative correlation with the flat at 390 nm. To better demonstrate the correlations, the spatial distributions of the model parameters and their best-correlated flats are compared in Figure 12. The correlation results are as expected.

1. At wavelengths where the photon absorption length L is smaller than or comparable to the electron absorption depth d (shorter than about 390 nm in the case of this work, where $d = 0.10$ μm), the small-scale flat mainly comes from the effect of charge collection efficiency, depending on both the electron absorption probability P and d.
2. At wavelengths where $L \gg d$ and $L \ll H$, around 650 nm in the case of this work, the effect of charge collection efficiency is small, and the CCD pixel thickness H does not matter; the small-scale flat is dominated by variations of the pixel effective area A.
3. At wavelengths where L is comparable to or larger than H, the effect of charge collection efficiency is small, and the CCD pixel thickness starts to matter, the small-scale flat mainly comes from variations of $H \cdot A$.

[16] We have tested several different regions, and the results are similar.

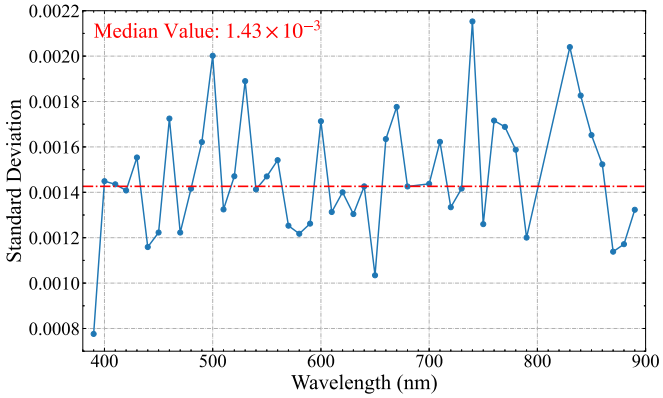

Figure 9. Standard deviations of the ratios of the observed to modeled small-scale flats of the center region as a function of wavelength. The median value is also noted and shown as the red dashed–dotted line.

In this work, we also performed a cubic polynomial fitting to wavelength-dependent small-scale flats for each pixel and compared the results with those of the physical model. Note that both methods have four free parameters for each pixel. The results are compared in Figure 13 for four randomly selected pixels. Both methods work well for the observed wavelength range. However, for shorter wavelengths (<400 nm), the results differ significantly. If our physical model is correct, it suggests that extrapolation of polynomial fitting results to shorter wavelengths is unreliable due to rapid variations of the charge collection efficiencies.

5. Discussion

The mini-JPAS camera does show wavelength-dependent small-scale flats, which are well explained by our model. The small-scale flats of the mini-JPAS camera come from at least two aspects. One is the inhomogeneities of the quantum efficiency (particularly charge collection efficiency) between adjacent CCD pixels. The other is the variations of the effective area and thickness of CCD pixels. The former dominates small-scale flats in short wavelengths, while the latter dominates in longer (visual and infrared) wavelengths.

The relative variation of the effective area between different pixels has a typical value of 0.44% (Figure 10), which cannot be ignored when precise photometric, astrometric, and shape measurements of astronomical objects are needed. Considering that the pixel scale is $0\farcs46$ pixel^{-1} ($0\farcs23$ physical pixel^{-1}) for the mini-JPAS camera and a typical seeing of $0\farcs71$ for the OAJ site (Moles et al. 2010), the effect of pixel area variations on photometry due to inappropriate small-scale flat-fielding is probably small (at a level of a few millimagnitudes). We note a strong anticorrelation between the A' and H' parameters. As shown in Figure 10, $A' \cdot H'$ has a much smaller dispersion value than A' and H' independently. The result suggests that the volumes of CCD pixels are more uniform than their areas and thicknesses.

Note that a pixel in this work corresponds to four physical pixels due to the binning in the readout process. To investigate the effect of binning on this work, we plot histogram distributions of different normalized model parameters after 2×2 binning in Figure 14. For parameters A', H', and $A' \cdot H'$, the sigma values decrease significantly by about a factor of 2. This is not surprising, as one would expect that variations of pixel area between neighbor pixels are anticorrelated (Baumer

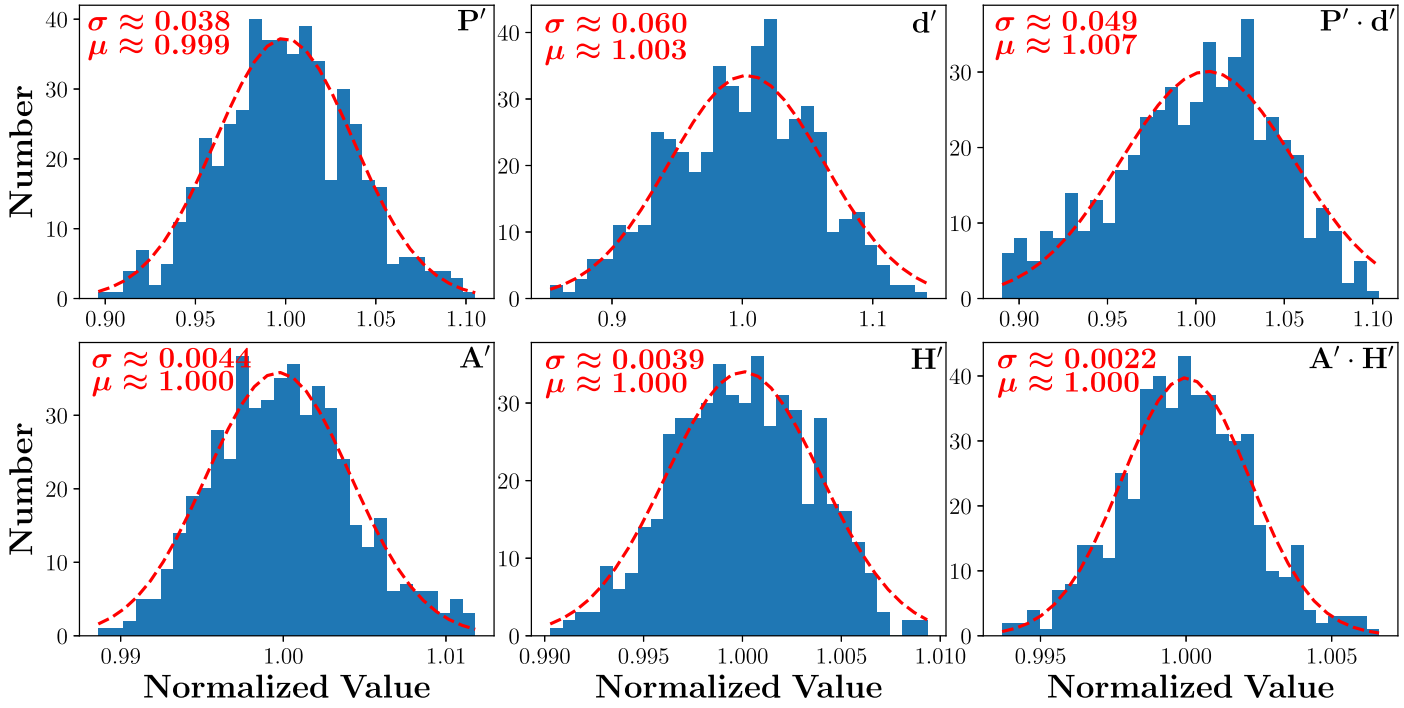

Figure 10. Histogram distributions of different normalized model parameters, as labeled in the top right corner of each panel. The red dashed curves are Gaussian fitting results, with sigma values labeled in the top left corners.

et al. 2017). Such anticorrelations can also be seen in the right panels of Figure 12. Therefore, we can infer that the true variations of A', H', and $A' \cdot H'$ for individual physical pixels are likely much larger than those shown in Figure 10. For P', the sigma value decreases slightly from 3.8% to 3.1%, suggesting a much weaker binning effect. This is probably because P has a larger variation scale, as can be seen in the top panels of Figure 12.

Due to the dependence of small-scale flats on wavelength, flat-fielding in the traditional way, which depends only on filters, may cause color terms in photometric calibration, particularly in blue and ultraviolet filters. Small-scale flat-fielding in slitless spectroscopic surveys may suffer similar problems. In order to achieve high-precision photometric/flux calibration, detailed modeling of wavelength-dependent variations of small-scale flats is needed. In this case, obtaining well-measured flats in a number of narrowband filters is necessary. The central wavelengths of the selected narrowband filters change slightly with the quantum efficiency curve of the CCD. A good sampling in the blue and ultraviolet wavelengths, where quantum efficiency varies rapidly, is suggested.

We adopted a set of reference values $P,\ d = [0.40,\ 0.10]$ in this work. To test the effect of different reference values, we selected another set of values $P,\ d = [0.50,\ 0.03]$ and compared them with the current results. Figure 15 plots correlations between the P and d parameters for the two sets of reference values. A strong correlation between P and d is seen for $P,\ d = [0.50,\ 0.03]$ in the top panel, while the correlation is much weaker for $P,\ d = [0.40,\ 0.10]$ in the bottom panel. The reason is that flats of short wavelengths, whose photon absorption depths are smaller than d, are needed to break the degeneracy between P and d. Here d is larger in the top panel (0.10 μm) than in the bottom (0.03 μm); therefore, the correlation is weaker. The result demonstrates the importance of flats at very short wavelengths.

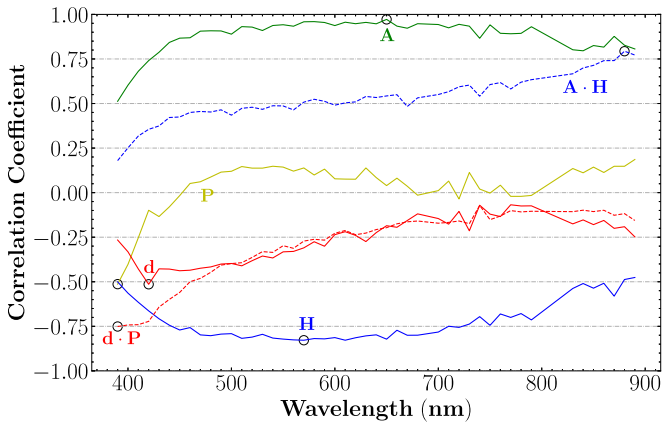

Figure 11. Correlation coefficients between model parameters and observed small-scale flats as a function of wavelength.

6. Conclusions

Using the unique data set provided by the flat fields of 47 narrowband filters used by the JPAS-Pathfinder, this paper addressed a question: how do the small-scale flats of a CCD camera depend on wavelength? Observationally, we detect variations from small-scale flats from different filters. The variations are stronger in shorter wavelengths. Small-scale flats of two filters close in central wavelengths are correlated, and we find that the closer the wavelengths, the stronger the correlation. Theoretically, we use a simple physical model to explain the observed wavelength-dependent variations of small-scale flats. The model considers the variations of charge

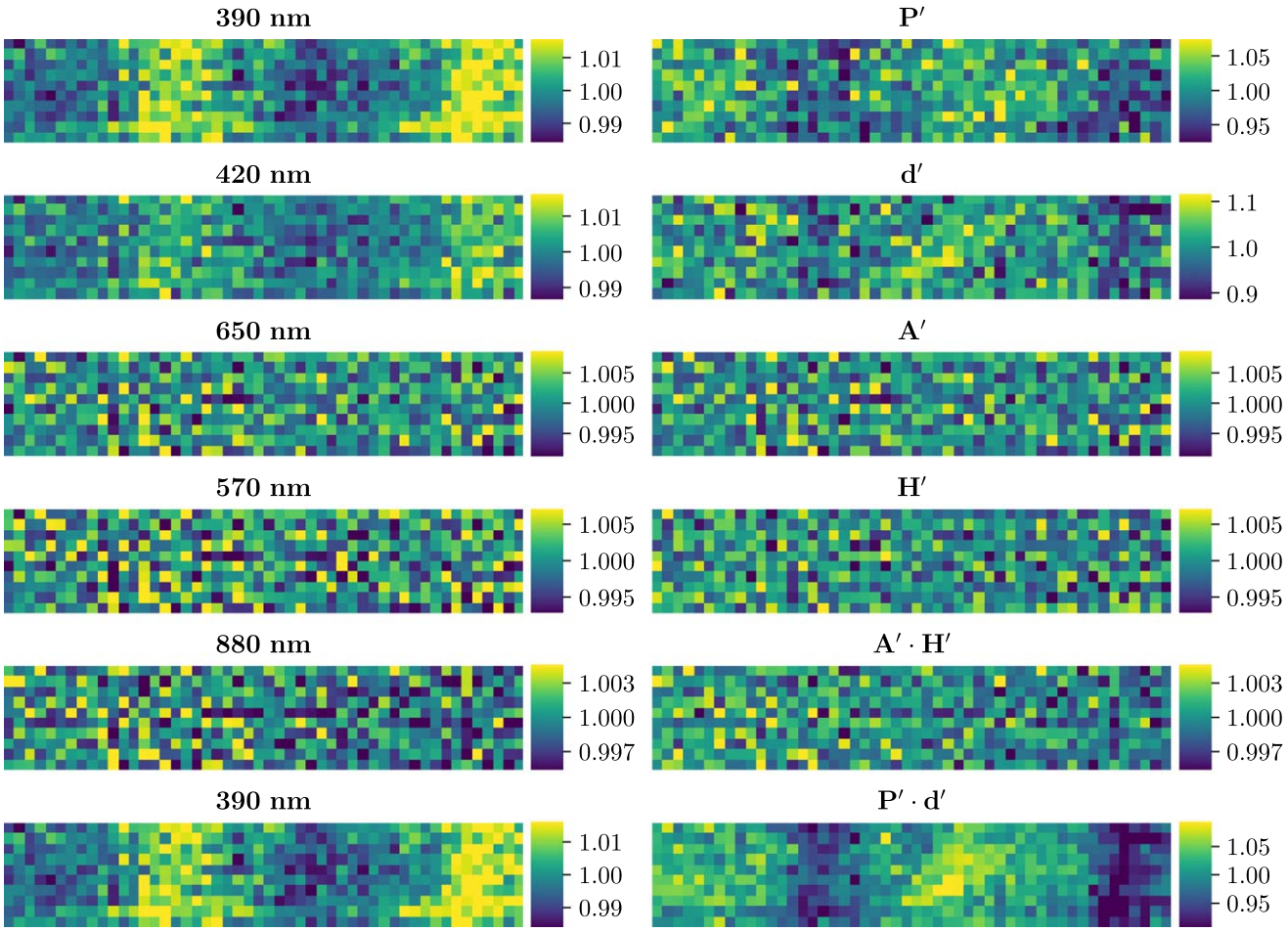

Figure 12. Model parameters (right panels) and their corresponding best-correlated observed small-scale flats (left panels).

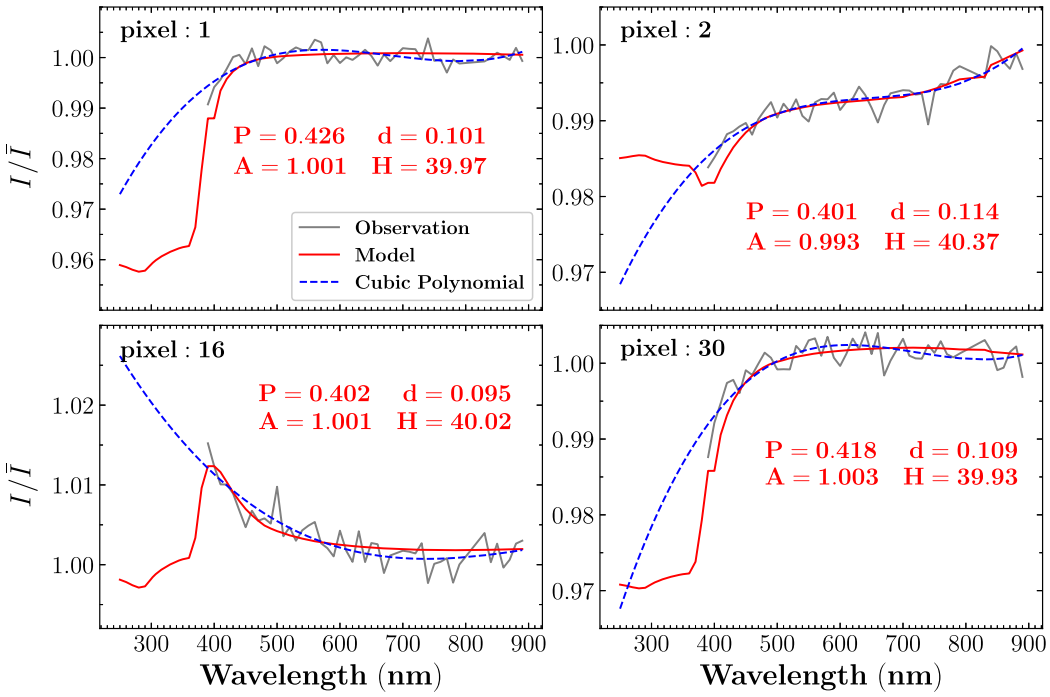

Figure 13. Observed (gray lines) and modeled (red lines) small-scale flats as a function of wavelength for four randomly selected pixels. The four model parameters for each pixel are labeled. For comparison, the results of cubic polynomial fitting are overplotted with blue dotted lines. Note the significant discrepancies between the red and blue lines at shorter wavelengths.

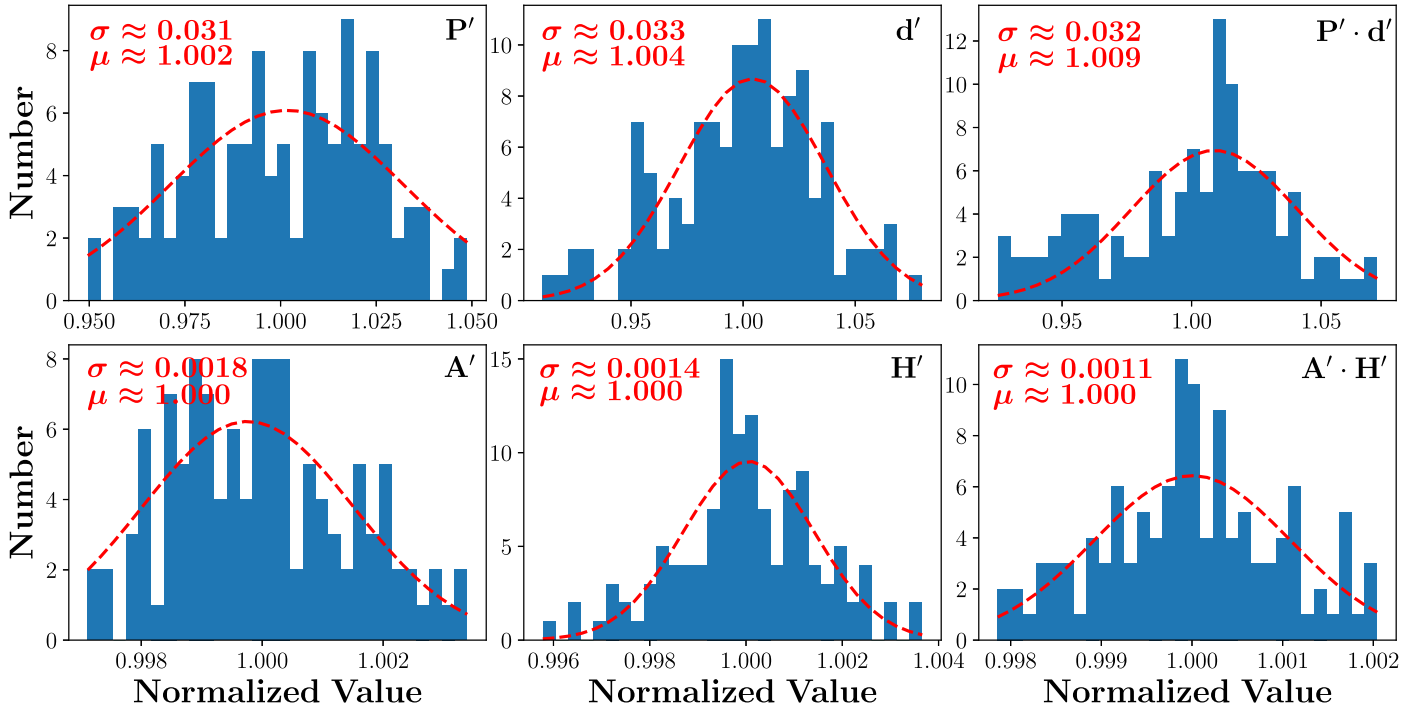

Figure 14. Histogram distributions of different normalized model parameters after 2 × 2 binning. The red dotted curves are Gaussian fitting results, with sigma values labeled in the top left corners.

collection efficiencies, effective areas, and thicknesses between pixels, with four free parameters (P, d, H, and A) to characterize each pixel. The observations are successfully reproduced to a precision of about 0.14%.

The model result shows that the wavelength-dependent variations of the small-scale flats of the mini-JPAS camera originate from two aspects. On one hand, the inhomogeneities of the quantum efficiency (particularly charge collection efficiency) between different CCD pixels dominate the variations at short wavelengths. On the other hand, the variations of the effective area and thickness of the CCD pixels are more important in longer (visual and infrared) wavelengths. The relative variation of the effective area between different pixels has a typical value of 0.44%, which cannot be ignored during flat-fielding when high-precision photometric, astrometric, or shape measurements of astronomical objects are needed. In order to achieve high-precision photometric calibration for imaging surveys or flux calibration for slitless spectroscopic surveys, detailed modeling of wavelength-dependent variations of small-scale flats is also needed to avoid color-dependent corrections, particularly in short wavelengths, where the CCD quantum efficiency curve varies rapidly.

In order to model the wavelength-dependent variations of small-scale flats, we find that different parameters are sensitive to flats of different wavelengths. At wavelengths where the photon absorption length L is smaller than or comparable to the electron absorption depth d, the small-scale flat mainly comes from the effect of charge collection efficiency, depending on both the electron absorption probability P and d. At wavelengths where $L \gg d$ and $L \ll H$, the small-scale flat is dominated by variations of the pixel effective area A. At wavelengths where L is comparable to or larger than H, the small-scale flat mainly comes from variations of $H \cdot A$.

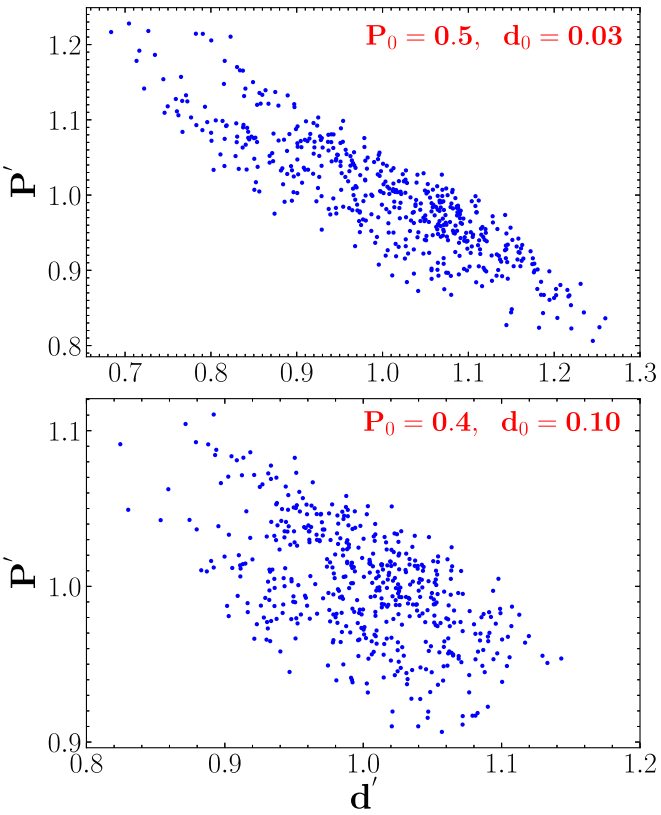

Figure 15. Correlations between P' and d' for two sets of initial reference values of P and d. Top: (P, d) = (0.50, 0.03). Bottom: (P, d) = (0.40, 0.10).

Therefore, a small number (around 10) of small-scale flats with well-selected wavelengths are sufficient to reconstruct small-scale flats in other wavelengths.

We acknowledge the anonymous referee for valuable comments that improved the quality of this paper. The PRNU model adopted in this work was developed as part of Mr. Baocun Chen's undergraduate thesis work under the supervision of H.Z. We acknowledge Drs. Stavros Akras, Alvaro Alvarez-Candal, Luis Alberto Díaz García, and Zhenya Zheng for a careful reading of the manuscript. This work is supported by the National Natural Science Foundation of China through projects NSFC 12173007 and 11603002, the National Key Basic R&D Program of China via 2019YFA0405503, and Beijing Normal University grant No. 310232102. We acknowledge the science research grants from the China Manned Space Project with Nos. CMS-CSST-2021-A08 and CMS-CSST-2021-A09. J.V. acknowledges the technical members of the UPAD for their invaluable work: Juan Castillo, Tamara Civera, Javier Hernández, Ángel López, Alberto Moreno, and David Muniesa.

Based on observations made with the JST/T250 telescope and JPCam at the Observatorio Astrofísico de Javalambre (OAJ) in Teruel, owned, managed, and operated by the Centro de Estudios de Física del Cosmos de Aragón (CEFCA). We acknowledge the OAJ Data Processing and Archiving Unit (UPAD) for reducing and calibrating the OAJ data used in this work.

Funding for the JPAS Project has been provided by the Governments of Spain and Aragón through the Fondo de Inversión de Teruel, European FEDER funding, and the Spanish Ministry of Science, Innovation and Universities, as well as by the Brazilian agencies FINEP, FAPESP, and FAPERJ and the National Observatory of Brazil. Additional funding was also provided by the Tartu Observatory and the JPAS Chinese Astronomical Consortium.

ORCID iDs

Kai Xiao https://orcid.org/0000-0001-8424-1079
Haibo Yuan https://orcid.org/0000-0003-2471-2363
Hu Zhan https://orcid.org/0000-0003-1718-6481
A. Marín-Franch https://orcid.org/0000-0002-9026-3933

References

Baumer, M., Davis, C. P., & Roodman, A. 2017, PASP, 129, 084502
Benitez, N., Dupke, R., Moles, M., et al. 2014, arXiv:1403.5237
Bonoli, S., Marín-Franch, A., Varela, J., et al. 2021, A&A, 653, A31
Brauneck, U., Sprengard, R., Bourquin, S., et al. 2018, JATIS, 4, 015002
DESI Collaboration, Aghamousa, A., Aguilar, J., et al. 2016, arXiv:1611.00037
Green, M. A., & Keevers, M. J. 1995, Prog. Photovolt.: Res. Appl., 3, 3
Howell, S. B. 2006, in Handbook of CCD Astronomy, ed. S. B. Howell (2nd ed.; Cambridge: Cambridge University Press)
Janesick, J., Klaasen, K., & Elliott, T. 1985, Proc. SPIE, 570, 7
Janesick, J. R. 2007, Photon Transfer DN → λ (Bellingham, WA: SPIE)
Kraft, D. 1998, A Software Package for Sequential Quadratic Programming, Technical Report, DFVLR-FB 88-28, Institut für der Flugsystemtechnik
LSST Science Collaboration, Abell, P. A., Allison, J., et al. 2009, arXiv:0912.0201
McEnery, J. 2021, AAS Meeting, 237, 327.01
Moles, M., Sánchez, S. F., Lamadrid, J. L., et al. 2010, PASP, 122, 363
Racca, G. D., Laureijs, R., Stagnaro, L., et al. 2016, Proc. SPIE, 9904, 99040O
Rajkanan, K., Singh, R., & Shewchun, J. 1979, SSEle, 22, 793
Stubbs, C. W., & Tonry, J. L. 2006, ApJ, 646, 1436
Verhoeve, P., Prod'homme, T., Oosterbroek, T., et al. 2014, Proc. SPIE, 9154, 915416
Wester, W. & Dark Energy Survey Collaboration 2005, in ASP Conf. Ser. 339, Observing Dark Energy, ed. S. C. Wolff & T. R. Lauer (San Francisco, CA: ASP), 152
York, D. G., Adelman, J., Anderson, J. E., et al. 2000, AJ, 120, 1579
Zhan, H. 2011, SSPMA, 41, 1441
Zhan, H. 2021, ChSBu, 66, 1290